



Overcoming pancreatic cancer immune resistance by codelivery of CCR2 antagonist using a STING-activating gemcitabine-based nanocarrier

Zhuoya Wan^{1,#}, Haozhe Huang^{1,#}, Raymond E. West III², Min Zhang¹, Bei Zhang¹, Xinran Cai¹, Ziqian Zhang¹, Zhangyi Luo¹, Yuang Chen¹, Yue Zhang¹, Wen Xie¹, Da Yang¹, Thomas D. Nolin², Junmei Wang³, Song Li^{1,*}, Jingjing Sun^{1,*}

¹ Center for Pharmacogenetics, Department of Pharmaceutical Science, University of Pittsburgh School of Pharmacy, Pittsburgh, PA, USA

² Department of Pharmacy and Therapeutics, University of Pittsburgh School of Pharmacy, Pittsburgh, PA, USA

³ Department of Pharmaceutical Sciences and Computational Chemical Genomics Screening Center, University of Pittsburgh School of Pharmacy, Pittsburgh, PA, USA

STING agonist has recently gained much attention for cancer treatment, but the therapeutic potential of STING agonist is hampered by STING-associated tumor immune resistance. In this work, guided by both bioinformatics and computer modeling, we rationally designed a “one stone hits two birds” nanoparticle-based strategy to simultaneously activate STING innate immune response while eliminating STING-associated immune resistance for the treatment of pancreatic ductal adenocarcinoma (PDAC). We discovered that the ultra-small sized micellar system based on gemcitabine-conjugated polymer (PGEM), which showed superior capacity of penetration in pancreatic tumor spheroid model and orthotopic tumor model, could serve as a novel “STING agonist”. The activation of STING signaling in dendritic cells (DCs) by PGEM increased both innate nature killer (NK) and adaptive anti-tumor T cell response. However, activation of STING signaling by PGEM in tumor cells also drove the induction of chemokines CCL2 and CCL7, resulting in immune resistance by recruiting tumor associated macrophage (TAM) and myeloid-derived suppressor cells (MDSCs). Through the combination of computer modeling and experimental screening, we developed a dual delivery modality by incorporating a CCR2 (the receptor shared by both CCL2 and CCL7) antagonist PF-6309 (PF) into PGEM micellar system. Our studies demonstrated that PGEM/PF formulation significantly reduced pancreatic tumor burden and induced potent anti-tumor immunity through reversing the CCL2/CCL7-mediated immunosuppression. Moreover, PGEM/PF sensitized PDAC tumors to anti-PD-1 therapy, leading to complete suppression/eradication of the tumors. Our work has shed light to the multi-faceted role of STING activation and provided a novel immunotherapy regimen to maximize the benefit of STING activation for PDAC treatment. In addition, this work paved a new way for bioinformatics and computer modeling-guided rational design of nanomedicine.

Keywords: STING; PF-6309; CCL2; Gemcitabine; PDAC

* Corresponding authors.

These authors equally contributed.

Introduction

Pancreatic ductal adenocarcinoma (PDAC) has the lowest 5-year survival rate (~8%) among cancers [1]. The lack of effective therapeutic strategy for PDAC is mainly attributed to its unique tumor microenvironment. The dense desmoplastic stroma not only restricts penetration of nanomedicine to the core of tumors, but also affects the infiltration of effector T cells, leading to an immunologically tolerant environment and driving treatment resistance [2]. Despite the success of immune checkpoint blockade (ICB) therapy in immunogenically “hot” tumors, it is less effective in treating immunogenically “cold” tumors such as PDAC [3]. Recently, activation of the innate immune system has demonstrated as a promising strategy to re-engage immune cold tumors to initiate anti-cancer immunity [4].

Stimulator of interferon genes (STING), an endoplasmic reticulum transmembrane protein, plays an important role in innate immunity against cancer. STING is activated when the cytosolic DNA (both exogenous and endogenous) is detected and processed by cyclic guanosine monophosphate-adenosine monophosphate synthase (cGAS) [5]. STING activation triggers downstream signaling cascades, such as recruitment and phosphorylation of TANK-binding kinase-1 (TBK1) and interferon regulatory factor (IRF3), resulting in the production of type I interferons (IFNs), particularly IFN- β and other chemokines, which promotes the activation of antigen presenting cells (APC) as well as the priming and infiltration of T-cell to tumor sites [6,7]. Tremendous efforts have been made in developing STING agonists for cancer immunotherapy [8]. The well-known agonists include cyclic dinucleotides (CDNs)-based agents and non CDN-based small molecules (e.g. DMXAA, G10 and α -Mangostin) [9]. Recent studies also demonstrated that some chemotherapeutic agents, such as platinum drugs, doxorubicin and low-dose camptothecin were able to activate the STING pathway via inflicting DNA double-strand breaks (DSBs) [10–12]. However, most STING agonists need to be administered intratumorally due to their metabolic instability and poor pharmacokinetic properties, which limited their clinical applications [13]. To address this issue, efforts are being made to develop STING agonists of improved physiochemical property and/or suitable formulations for systemic administration [14,15]. Nevertheless, increasing evidence has shown that the STING activation in tumor immunity is multi-faceted. Despite that Type I interferons and STING-inducible cytokines play important roles in directing dendritic cells (DC) function and T cell priming to initiate anti-tumor response, overproduction of certain cytokines was found to result in immune resistance as well as tissue damage and pathological inflammation [16]. For example, Chung et al reported that aberrant packaging of the mitochondrial DNA (mtDNA) could activate cGAS-STING innate immune pathway, resulting in IFN production and cytokine release, which contributes significantly to cell death and kidney failure [17]. In addition, it has been reported that radiation-induced STING activation led to increased expression of chemokines CCL2 and CCL7, which played an important role in tumor radio-resistance [18].

CCL2 and CCL7 are produced by many types of cancer cells including PDAC cells, which are major tumor-derived factors

responsible for recruiting immunosuppressive immune cells and promoting tumor progression and metastasis. Thus, CCL2 and CCL7 might be involved in both intrinsic and acquired resistance of tumor cells to various treatments including chemotherapy [19]. CCL2 and CCL7 shared the same functional receptor CCR2, which is an attractive target for cancer therapy [20,21]. However, current investigations mainly focus on the strategies to activate STING, developing an effective strategy to simultaneously activate STING while counteracting the overproduction of pro-immune resistance chemokines has rarely been reported.

In this work, guided by RNA sequencing (RNAseq), we discovered that a gemcitabine (GEM)-conjugated polymer (PGEM) was able to activate cGAS-STING innate immune pathway. This polymer could self-assemble into an ultra-small sized particles (~13 nm) that served as a prodrug carrier for efficient loading of a wide variety of drugs [22]. The superior penetration capability of small sized PGEM carrier was confirmed in pancreatic tumor spheroid model and orthotopic pancreatic tumor model. However, we also discovered that the STING activation by PGEM led to increased expression of CCL2 and CCL7, resulting in tumor immune resistance. With the guidance of molecular dynamic simulations, we developed a “one stone hits two birds” formulation by incorporating an “optimally” paired CCR2 antagonist into PGEM carrier to simultaneously activate STING and overcome immune resistance to further improve the overall therapeutic effect (Scheme 1). The potential of PGEM/PF in sensitizing PDAC to programmed death-1 (PD-1) immune checkpoint blockade was also investigated.

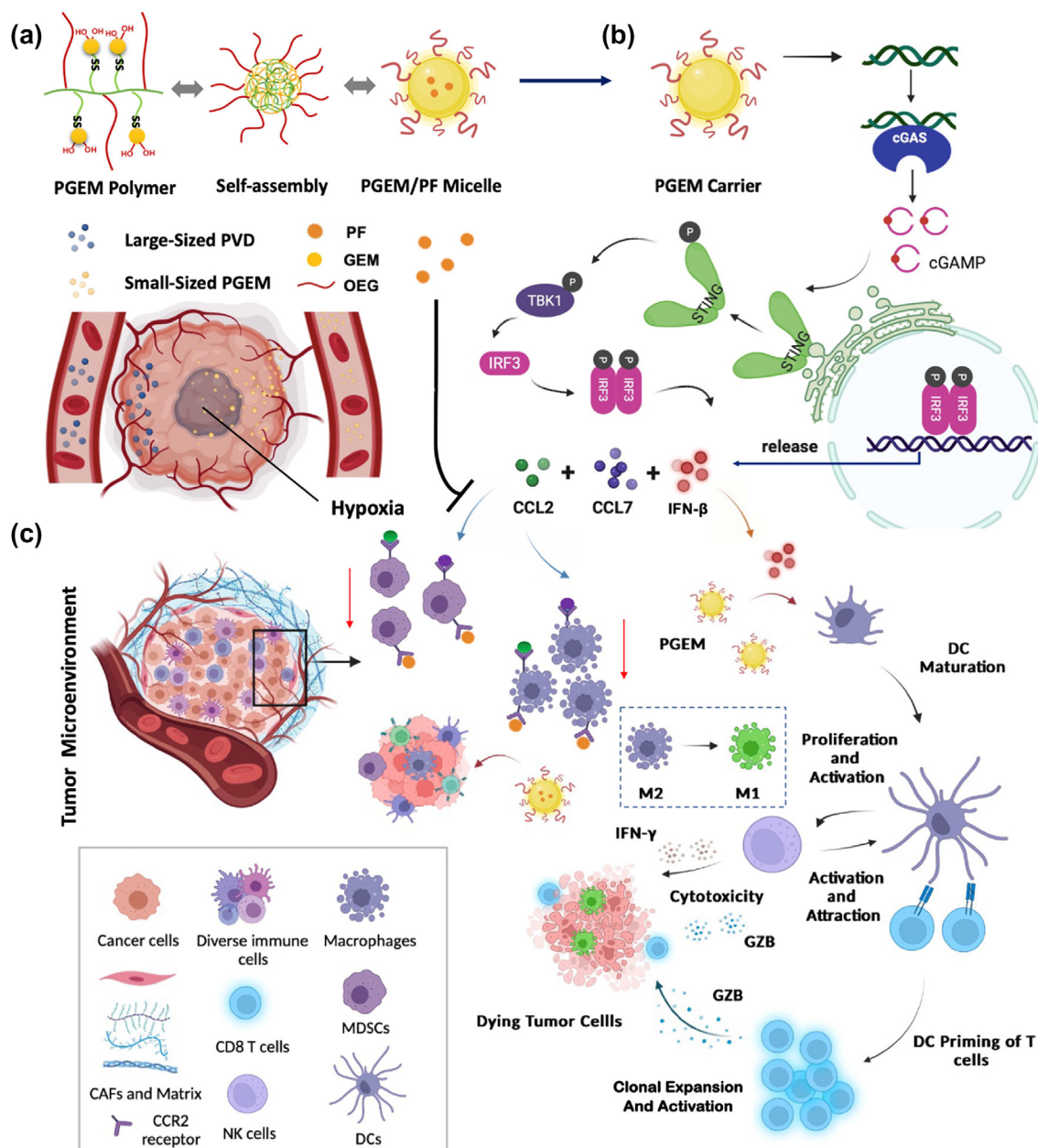
Materials and methods

Materials

Gemcitabine (GEM) was obtained from LC Laboratories (MA, USA). PF-04136309 (PF) and Bindarit (Bind) were purchased from Medchemexpress LLC (USA), BMS813160 (BMS) was purchased from Selleck USA. Vinylbenzyl chloride, potassium carbonate (K_2CO_3), azobisisobutyronitrile (AIBN), sodium hydroxide (NaOH), di-tert-butyl decarbonate, 1,4-dioxane, N,N-diisopropylethylamine (DIPEA), triethylamine (TEA), 4-cyano-4-[(dodecylsulfanyltiocarbonyl) sulfanyl] pentanoic acid, dimethylformamide (DMF), tetrahydrofuran (THF), dimethyl sulfoxide (DMSO), N-hydroxy succinimide (NHS), and poly(ethylene glycol) methyl ether methacrylate (OEGMA) were purchased from Fisher Scientific. AIBN was purified by recrystallization in ethanol according to the literature [23]. 1-(3-Dimethylaminopropyl)-3-ethylcarbodiimide HCl (EDC-HCl) and 1-hydroxybenzotriazole (HOBT) were purchased from GL Biochem (Shanghai, China). Dulbecco's Modified Eagle's Medium (DMEM) and 3-(4,5-dimethylthiazol-2-yl)-2,5-diphenyl tetrazolium bromide (MTT) was bought from Sigma-Aldrich (MO, USA).

Cells and animals

Murine pancreatic cell line Panc02 was obtained from ATCC (Manassas, VA). KPC cell line was kindly gifted by Professor Wen Xie's lab at University of Pittsburgh. Panc02 was routinely cultured in DMEM supplemented with 10 % fetal bovine serum (FBS) and 100 U/mL penicillin/streptomycin at 37°C in a humidified environment with 5 % CO_2 . KPC cells were cultured in



SCHEME 1

PGEM/PF micelles exert potent anti-tumor efficacy by modulating TME and amplifying STING activation. (a) Preparation of small-sized PGEM/PF micelles that effectively penetrated into PDAC solid tumors following systemic administration. (b) PGEM boosted STING activation and subsequent TBK1 phosphorylation and IRF3 phosphorylation, resulting in induction of IFN β along with CCL2 and CCL7. (c) The PGEM-induced IFN β expression significantly enhanced antitumor immunity through promoting DC maturation and activating both innate immunity (NK cells) and adaptive anti-tumor immunity (CD8 T cells). Meanwhile, both CCL2 and CCL7 help to recruit tumor associated macrophages (TAM) and MDSCs through acting on CCR2. PF released from PGEM/PF micelles further improved the antitumor immunity through reversing the immunosuppressive TME mediated by STING activation.

DMEM (high glucose without sodium pyruvate) with 10 % FBS and glutamine (2 mM) as reported [24].

Female C57/BL6 mice (4–6 weeks old) were purchased from Jackson Laboratory. All animal experiments were conducted following the guidelines of the Institutional Animal Care and Use Committees (IACUC) of University of Pittsburgh.

Preparation and characterization of drug loaded PGEM micelles

PVD polymer was synthesized by controlled Reversible Addition Fragmentation Chain Transfer (RAFT) polymerization as described previously [22]. PGEM polymer was synthesized by conjugating GEM to PVD polymer backbone via EDC/HOBT coupling [22]. The polymer structures were characterized by FT-IR.

Blank and CCR2 inhibitors-loaded PGEM micelles were prepared by film hydration method. Briefly, PGEM polymer and CCR2 inhibitors (PF, BMS, and Bind) were mixed in dichloromethane/methanol with various carrier/drug ratios. A thin film was formed after completely removing all the organic solvent via evaporation method. The films were then hydrated with phosphate-buffered saline (PBS) solution to give PF-, BMS-, and Bind-loaded PGEM micelles, respectively. 1,1'-Diocadecyl-3,3',3'-Tetramethylindotricarbocyanine Iodide (DiR) or rhodamine loaded PGEM micelles and PVD micelles were prepared similarly. Drug loading capacity (DLC) and drug loading efficiency (DLE) were determined by HPLC and calculated according to the following equations:

$$\text{DLC (\%)} = [\text{weight of drug loaded}/(\text{weight of polymer} + \text{drug used})] \times 100.$$

$$\text{DLE (\%)} = (\text{weight of loaded drug}/\text{weight of input drug}) \times 100.$$

Preparation of three-dimensional tumor spheroids

Panc02 cells and KPC cells were seeded in the Corning 96-well ultra-low-attachment plates with DMEM containing 10 % FBS and 6 µg/mL of Collagen, respectively. The tumor spheroids were formed after incubation for three days at 37 °C with 5 % CO₂. Then, the prepared tumor spheroids were transferred to a new 96-well plate with 100 µL of fresh media containing rhodamine-loaded PGEM and PVD nanoparticles. After incubation for 16 h, the tumor spheroids were washed with cold PBS and the z-stack images were obtained by laser confocal microscopy.

Establishment of orthotopic KPC pancreatic tumor model

Orthotopic KPC xenograft model was established according to previous publication [25]. Briefly, the animals were anesthetized with continuously isoflurane, and the surgical site was sterilized by repetitive application of betadine and 70 % ethanol. The surgery was performed in an appropriate position: animals were placed on a water heating pad and the surgical site was draped with sterile gauze. In brief, a surgical incision of 0.5 ~ 0.7 cm was made in the left flank of mice to expose the injection site, followed by an injection of 50 µL of DMEM/Matrigel (1:1, v/v) containing 1×10^6 KPC cells into the tail of the pancreas. The surgery area was then closed carefully. The mice were kept on the warming pads until full recovery from the anesthesia status and then transferred to clean cages and maintained in pathogen-free condition.

Bulk RNA-Seq analysis

The Panc02 tumor-bearing mice were intravenously injected with saline, GEM and PGEM once every-three days for 3 times, respectively. One day after last injection, the tumors were harvested for RNA sequencing (RNA-seq), which was performed by the Health Sciences Sequencing Core at Children's Hospital at University of Pittsburgh. RNA-Seq libraries were sequenced as 75-bp paired-end reads at a depth of ~ 73–77 million reads per sample. Reads were mapped to the mouse genome (GRCm38) using STAR Aligner 2.6.1a [26]. Gene expression quantification and differential expression analysis was performed on Saline, GEM, and PGEM treated tumor samples using RSEM 1.3.1 [27]

and Cuffdiff of Cufflinks 2.2.1 [28]. Volcano plots were generated to show the overall differential expression between pairwise comparisons among these three groups, where the x-axis indicates the log-transformed fold changes (log2FC) and the y-axis indicates the corresponding negative log-transformed p-values ($-\log_{10}(\text{p-value})$). The Gene Set Enrichment Analysis (GSEA) [29,30] was further performed based on the gene lists ranked by the log2FC among three groups.

Western blotting

Western blotting was performed to evaluate the STING activation in cultured Panc02 cells. Cells grown in six-well plates with 80 % confluency were treated with saline, free GEM, PGEM micelles, and PVD micelles, respectively, for 48 h. Then, the cultured Panc02 cells were washed twice with pre-cooled PBS and lysed in Pierce™ RIPA buffer for 30 min in 4 °C. Protein concentrations were determined by BCA method, and equal amounts of total protein lysate were resolved on a 10 % SDS-PAGE and subsequently transferred to a nitrocellulose membrane. Membranes were blocked with 5 % non-fat milk in PBS for 1 h prior to incubation with various antibodies targeting IRF3, P-IRF3, STING, P-STING, and Cyclin B dissolved in PBST (DPBS with 0.1 % Tween 20) overnight at 4 °C. The blots were washed with PBST and then probed with goat antirabbit IgG for 1 h at room temperature followed by chemiluminescence detection by SuperSignal™ West Fento Maximum Sensitivity Substrate. β-Actin or GAPDH was used as a loading control.

Immunofluorescence microscopy

Panc02 cells were seeded on chamber slides and treated with saline, free GEM, PGEM micelles, and PVD micelles, respectively. For all immunofluorescence staining, cells were washed in PBS, fixed in 4 % formaldehyde/PBS for ten minutes at room temperature (RT) and permeabilized in 0.25 % Triton/PBS for 20 minutes at RT. Blocking was performed in 5 % BSA/0.1 % Triton/PBS for 30 minutes, followed by incubation with primary antibodies in blocking buffer for one hour at 37 °C incubator. Cells were washed in PBS and incubated with secondary antibodies in blocking buffer for one hour at RT, followed by washing and mounting on coverslips using ProLong Gold antifade reagent with DAPI. Cells were imaged using confocal microscope at the specified magnification. For picogreen-cGAS staining, cells were incubated with pico488 DNA quantification reagent for 2 hours at 37 °C. For γH2AX staining, permeabilized cells were blocked in Serum-free DAKO Protein Block for one hour at RT. Cells were incubated in primary antibody (γH2AX, 1:500; anti-HA, 1:100) in DAKO antibody diluent at 4 °C overnight on a rocker platform.

qRT-PCR

Panc02 cells grown in six-well plates were treated with saline, free GEM, PGEM micelles, and PVD micelles, respectively, for 48 h. Then, RNA was isolated using the PureLink RNA kit (Invitrogen) and reverse transcribed using the High-Capacity cDNA Reverse Transcription Kit (Applied Biosystems) based on the manufacturer's guidelines. qPCR was performed using Power SYBR Green PCR MasterMix (Applied Biosystems) in a QuantStudio 3 Real-Time PCR System (Applied Biosystems). The primer sequences were listed in Table S1.

In a separate study, Panc02 cells grown in six-well plates were treated with PGEM for 72 h. One day after adding PGEM into the wells, control siRNA (siNC) or STING siRNA (siSTING) was added into the wells without changing the medium, and incubated for 48 h. Then the RNA was extracted, and CCL2, CCL7 and ISG15 expression levels were detected as described above. In another study, we evaluated whether CCL2, CCL7 and ISG15 were induced by type I IFNs [43]. Panc02 cells grown in six-well plates were treated with PGEM for 72 h. One day after adding PGEM into the wells, isotype control (10 µg/mL) or IFNAR1 antibody (10 µg/mL) was added into the wells without changing the medium, and incubated for 48 h. Then, the RNA was extracted subjected to qRT-PCR analysis of the mRNA expression levels of CCL2, CCL7 and ISG15.

Molecular simulation systems

A single copy of the PGEM polymer consists of 32 residues from four residue types, which are PG, EM, NPG (N-terminal PG) and CEM (C-terminal EM) (Fig. 4a). Each residue has the hydrophilic and hydrophobic parts. The hydrophilic part tends to be exposed to water, while the hydrophobic part tends to form a hydrophobic core of a micelle structure. For PG and NPG, the hydrophilic part is the polyethylene glycol (PEG) repeat units, and the other atoms belong to the hydrophobic part. For EM and CEM, the hydrophilic part is the substructure containing gemcitabine and the adjacent amide functional group, and the other atoms belong to the hydrophobic part. The four residues and the three drugs were described by the GAFF [31] force field. Specifically, we performed *ab initio* calculations (B3LYP/6-31G*/HF/6-31G*) using Gaussian 16 package [32] to obtain electrostatic potentials to derive point charges, and then applied Antechamber software package [33] to generate residue topologies. As there is no experimentally determined structure for PGEM, we generated an initial structure which has an extended conformation. Although the numbers of PG and EM residues are known from experiment, the exact sequence of the polymer is unclear. Our PGEM model maximally separates the two types of non-terminal residues and the sequence is as the follows: NPG-EM-EM-EM-PG-EM-EM-PG-EM-EM-EM-PG-EM-EM-PG-EM-EM-PG-EM-EM-PG-EM-EM-PG-EM-EM-EM-PG-EM-EM-EM-PG-EM-EM-CEM.

Molecular dynamics simulations

We applied a series of sequential molecular dynamics (MD) simulations to obtain the micelle structure formed by a single copy of polymer, and then studied how multi-drug molecules interacted with the polymer in explicit water. In Step 1, the extended conformation of the polymer was collapsed in explicit water during the 100 nanoseconds (ns) simulation. Then a Generalized Born molecular dynamics (GBMD) simulation was performed to exclude the trapped water molecules and accelerate micelle structure formation. Note that the initial conformation of this step came from the last snapshot of Step1. Next, in Step 3 we performed 200-ns MD simulations in explicit water environment to sample an isothermal-isobaric ensemble of the polymer for the followed free energy analysis. Similarly, the initial conformation of this step came from the last MD snapshot of Step 2. Next, in Step 4 we carried out 220-ns MD simulations for the systems containing a copy of polymer and 8 copies of a drug molecule. Ini-

tially, the 8 copies of drug molecules were placed at the vertices of a cube (edge length = 50 Å) with the polymer being placed in the center. The polymer structure was from the last snapshot of Step 3. Finally, for the sake of free energy calculations, a 200-ns MD simulation was performed for a single copy of drug molecule in aqueous solution (Step 5). In total, three drug molecules were studied in this work including Bindarit, BMS813160, and PF-04136309. For both GBMD and explicit water MD simulations, the time step of integrating the Newton's equation of motion was set to 2 femtoseconds, and desired temperature and pressure were set to 298 K and 1 bar, respectively. All MD simulations were performed using the pmemd.cuda program in AMBER 18 [34].

Free energy analysis

500 snapshots from the sampling phase (after 50 ns) of a trajectory were collected for free energy calculations. An internal program was applied to calculate the MM-PBSA-WSAS free energies of the polymer, the drug and the complex formed by the polymer and 8 drug molecules. For a molecular system, the polar solvation free energy was calculated with the Delphi 95 software [35,36], using the interior and exterior dielectric constants of 1.0 and 80.0, respectively. The nonpolar solvation free energy was estimated using the solvent accessible surface area (SAS) as detailed elsewhere [37,38]. The conformational entropy of the system was predicted using WSAS, a weighted solvent-accessible surface area approach [39]. To calculate the binding free energy between the polymer and 8 drug molecules, we adopted the “three-trajectories” protocol [39], for which we calculated the free energies of the polymer, the complex, and the drug using three MD trajectories separately sampled in Steps 3, 4 and 5. The MM-PBSA-WSAS binding free energy was calculated using the following formula: $\Delta G_{\text{binding}} = G_{\text{complex}} - (G_{\text{polymer}} + 8 \times G_{\text{drug}})$. Note that the complex contains 8 copies of the drug molecule.

MTT assay

Panc02 cells were seeded in 96-well plates at a density of 1500 cells/well with 100 µL of complete culture medium (DMEM with 10 % FBS and 1 % streptomycin/penicillin). After overnight incubation, Panc02 cells were treated with various concentrations of saline, free PF, free BMS, free Bind, free GEM, free GEM + PF, PGEM, PGEM/PF, PGEM/BMS, and PGEM/Bind micelles. After 96 h, the cytotoxicity was determined by MTT assay. The absorbance of each well was measured at 590 nm and the cell viability was determined via the following formula: $(\text{OD}_{\text{treated}} - \text{OD}_{\text{blank}}) / (\text{OD}_{\text{control}} - \text{OD}_{\text{blank}}) \times 100 \%$.

Release of PF from PGEM/PF micelles

The release of PF from PGEM/PF micelles was examined at 37 °C via a dialysis method with free PF as a control. PF-loaded PGEM micelles was transferred into a dialysis bag with MWCO of 3500 Da, which was then incubated in 50 mL PBS with 0.5 % (w/v) tween 80 under gentle shaking. At specific time intervals, all the PBS solution outside the dialysis bag was withdrawn and replaced with another 50 mL of fresh solution. The PF concentrations in the solution were determined by HPLC [40].

In vivo anti-tumor study

The antitumor effect was evaluated in syngeneic mice bearing Panc02 tumors. In brief, 1×10^5 Panc02 cells were inoculated into the right flank of female C57BL/6 mice. When the tumor volume reached $\sim 50 \text{ mm}^3$, the mice started to receive different treatments. To screen the best CCR2-inhibitor loaded PGEM micelles, PF-, Bind-, and BMS-loaded PGEM micelles (10 mg/kg for CCR2 inhibitor) were intravenously administered three times at an interval of three days, while saline and PGEM micelles worked as control groups. In a separate study, the synergistic tumor inhibition effect of PF and GEM was evaluated by intravenously injecting saline, free GEM, free PF, free GEM + PF, PGEM, and PGEM/PF (GEM: 20 mg/kg; PF: 10 mg/kg), respectively, into the Panc02 tumor-bearing mice. These treatments were also performed three times at an interval of three days. The tumor volumes and body weights were continuously monitored. At the endpoint, the tumor tissues and major organs were fixed in 10 % formalin and dehydrated. Then they were embedded in paraffin and sectioned, followed by H&E staining with for histopathological examination. The biochemical parameters, including WBCs, RBCs, Hb, AST, ALT, and creatinine, were evaluated for safety profiles. The effect of PGEM/PF on the inhibition of lung metastasis of pancreatic cancer was also evaluated. A pulmonary metastasis model of pancreatic cancer was established by injecting KPC cells via tail vein. On day 10 following tumor cell inoculation, mice were i.v. administered with saline, free GEM + PF, PGEM, and PGEM/PF, respectively. The treatment was performed at day 10, day 14, and Day 18, and the mice were sacrificed at day 20.

In a separate study, the survival of the tumor-bearing mice was examined following various treatments, including saline, free GEM + PF, PGEM, and PGEM/PF (PF dose: 20 mg/kg). The treatments were performed once every 4 days for 3 times. The end point of survival was defined as animal death or when the tumor volume reached $\sim 2000 \text{ mm}^3$. The survival rate was plotted as Kaplan Meier curves.

To test the combination effect of PGEM/PF formulation with anti-PD-1, Panc02 tumor-bearing mice were treated with anti-PD-1 (clone RMP1-14, BioXCell), PGEM/PF or the combination of PGEM/PF formulation and anti-PD-1 (100 μg anti-PD-1 per mouse, *i.p.* and 5 mg/kg PF, *i.v.*). The tumor growth was followed every 4 days and tumors were weighed at the completion of the experiment.

Biodistribution and tumor retention of PGEM/PF

The distribution and retention of drug in the tumors was performed in the orthotopic KPC model, which was established according to previous publication [25]. At 3 weeks post inoculation of KPC cells, the mice were intravenously injected with DiR-loaded PGEM micelles at a DiR concentration of 0.06 mg/mL. At 24 h post injection, the tumors and major organs were harvested and the biodistribution of PGEM NPs was evaluated by near infrared fluorescence (NIR) imaging using IVIS 200 system (Perkin Elmer, USA). In a separate study, the tumor retention of PGEM NPs was followed by NIR imaging at indicated time points (0 h, 24 h, 48 h, 72 h, 96 h, 120 h, 144 h, and 168 h).

For the PF quantitation, the tissues were collected and homogenized with PBS [40]. The homogenized tissue samples were cen-

trifuged, and 75 μL of the supernatant was transferred to a tube, to which 150 μL methanol containing the internal standard (apixaban- ^{13}C - d_3) was added. After protein precipitation, the PF concentration was detected by LC-MS/MS. Chromatographic separation was performed using a Waters Cortecs T3 column ($2.1 \times 50 \text{ mm}$, $1.6 \mu\text{m}$). An isocratic gradient was used for PF with a total runtime of 6 minutes using the mobile phases water with 0.1 % formic acid (A) and acetonitrile (B).

Quantification of tumor-infiltrating lymphocytes by flow cytometry

Syngeneic C57BL/6 mice bearing Panc02 tumors received various treatments (saline, free GEM, free PF, free GEM + PF, PGEM, and PGEM/PF) via i.v. administration every-three days for three times. Tumors were collected at 24 h following the last treatment. Single cell suspensions were prepared according to previous literature [41]. Then the cells were stained with various antibodies (Table S2) for flow cytometry analysis. For intracellular cytokine (IFN- γ and GZB) staining, cells were stimulated with PMA (100 ng/mL) and Ionomycin (500 ng/mL) for 5 h in the presence of Monensin. Cells were fixed/permeabilized using the BD Cytofix/Cytoperm kit prior to cell staining. Then, the fixed/permeabilized cells were suspended in residual Intracellular Staining Perm Wash Buffer and a predetermined optimum concentration of fluorophore-conjugated antibody of interest was added (e.g. PE anti-IFN- γ) for 30 minutes. The data were analyzed using FlowJo software (Tree Star Inc). The percentage of cytokine (IFN- γ or GZB)-producing NK and CD8 $^+$ T cells was gated under total NK and CD8 $^+$ T cells, respectively, which represents the percentage of total NK or CD8 $^+$ T that are IFN- γ or GZB positive.

In a separate study, C57BL/6 mice bearing GFP-Panc02 tumors were treated with saline, GEM and PGEM, respectively, every-three days for three times. The tumors were harvested at 24 h following the last treatment, and the single cell suspension was prepared and stained with various antibodies. Compensation was performed using both single color stains and isotype controls, in line with the published protocol [41]. In brief, Phospho-TBK1/NAK (Ser172) (D52C2) XP $^{\text{R}}$ Rabbit mAb (PE Conjugate) or concentration matched Rabbit (DA1E) mAb IgG XP $^{\text{R}}$ Isotype Control (PE Conjugate) was used for flow cytometric analysis. Similarly, Phospho-IRF-3 (Ser396) (D6O1M) Rabbit mAb (Alexa Fluor $^{\text{R}}$ 647 Conjugate) or concentration matched Rabbit (DA1E) mAb IgG XP $^{\text{R}}$ Isotype Control (Alexa Fluor $^{\text{R}}$ 647 Conjugate) was used for Flow cytometric analysis.

Neutralization of immune cells and cytokines

To study the contribution of NK and CD8 $^+$ T cells to the antitumor effect, five mice in each group were intraperitoneally injected with 200 μg of anti-CD8a (clone 2.43, Bio X Cell) or anti-mouse NK1.1 (clone PK136, Bio X Cell) antibody or their matched isotype controls four times (days 6, 9, 12, and 15) after tumor inoculation following previous reported method [42]. In addition, the type I IFNs signaling was blocked using the antibody against the type I interferon receptor (IFNAR-1) to investigate whether the efficacy of PGEM therapy is dependent on type I IFNs. Antibody was administered by intraperitoneal injection on days 6 and 7 at a dose of 200 μg per mouse after tumor inoculation. The tumor volumes and body weights were contin-

uously monitored. At the endpoint, the tumor weights were measured.

Results and discussions

PGEM showed superior tumor penetration in multiple PDAC models

GEM, a cytidine analogue, is the first-line chemotherapeutic drug for the treatment of pancreatic cancer and works through inhibiting DNA replication [44]. However, limited clinical benefits from GEM are achieved because of its inefficient delivery and the rapid degradation by cytidine deaminase (CDA). Nanotechnology offers the advantages of improving drug delivery, protecting GEM from inactivation by deaminase and reducing the toxicity [45–47]. However, PDAC is known to be poorly vascularized with small pore sizes (~50–60 nm), which limits the extravasation of large nanoparticles [48]. In addition, PDAC has dense stroma that further limits the penetration of large nanoparticles into the tumor core. Nab-paclitaxel has been reported to destroy the cancer-associated fibroblasts (CAF) and increase the drug penetration and intratumoral accumulation [49]. However, the stroma depletion could enhance the spread of tumor cells, leading to compromised therapeutic efficacy [50]. Increasing evidence has shown that smaller nanoparticles (≤ 30 nm) were much more effective in penetrating stroma-abundant pancreatic tumors without destroying the stroma [51]. Recently, we synthesized a unique PVD polymer backbone, and found that conjugation of GEM to PVD backbone dramatically decreased the particle size from ~160 nm to ~13 nm, yielding an ultra-small prodrug polymeric carrier (PGEM) (Fig. S1) [22]. The structures of the PVD and PGEM polymers were characterized by FT-IR (Fig. S2). Compared to PVD, PGEM showed strong broad O–H stretching at 3600–3100, suggesting the successful conjugation of GEM to PVD backbone.

In this work, the tumor penetration of PGEM nanocarrier was firstly evaluated by using Panc02 cell- and KPC cell-derived tumor spheroids. To mimic the tumor microenvironment *in vivo*, the spheroids were composed of both the tumor cells and collagen matrix. The spheroids were treated with rhodamine-loaded PGEM and PVD micelles, respectively, for visualization by Confocal Z-stacks scanning with 20 μ m Z-intervals (Fig. 1a). As shown in Fig. 1b–c, PVD/Rhodamine micelles (~160 nm) were mainly localized around the peripheral area with essentially no signals in the core. In contrast, the PGEM micelles (~13 nm) showed significantly stronger ability to penetrate the tumor and the signals were distributed throughout the entire spheroids.

The tumor targeting efficiency of PGEM carrier was further evaluated by near-infrared fluorescent (NIR) optical imaging using the DiR probe. The DiR-loaded PGEM micelles were intravenously injected into the orthotopic KPC tumor-bearing mice, which were established by injecting KPC cells into the tail of the pancreas (Fig. 1d). IVIS live imaging showed that DiR-loaded PGEM micelles were mainly accumulated in the pancreas tumor sites at different time points post injection (Fig. S3). The mice were sacrificed at 24 h, and it was further confirmed that DiR-loaded PGEM micelles were preferentially accumulated at the pancreas tumor site (Fig. 1e–f). We also evaluated the reten-

tion time of PGEM nanocarrier in the tumor tissues. The signals slowly decreased with time, and over 50 % of signals remained in the tumors at 96 h.

PGEM activated the cGAS-STING pathway

PGEM has been shown to significantly inhibit tumor growth in several tumor models, including Panc02, CT26 and PDX models [22]. To gain mechanistic insights for the PGEM-mediated anti-tumor response, RNA sequencing (RNA-Seq) was performed on Panc02 tumor tissues treated with saline, GEM, and PGEM, respectively. Four hundreds and eighty-nine (489) genes were significantly downregulated and 416 genes were significantly upregulated after GEM treatment, while 407 genes were significantly downregulated and 461 genes were significantly upregulated after PGEM treatment (Cuffdiff $P < 0.05$). Through Gene Set Enrichment Analysis (GSEA) [29,30], we found that PGEM treatment significantly downregulated several signaling pathways critically involved in the initiation and progression of PC [52], including MTORC1_SIGNALING, HYPOXIA, HEDGEHOG_SIGNALING, NOTCH_SIGNALING and KRAS_SIGNALING (Fig. S4).

It is important to note that cytosolic DNA sensing signaling, interferon-alpha response, and NF κ B signaling pathway (Fig. 2a, Fig. S5) were upregulated by PGEM comparing to GEM treatment. As the binding of cytosolic DNA with cGAS has been shown to activate cGAS-STING pathway and trigger downstream pathways such as type I interferon and nuclear factor κ B (NF- κ B) signalings [53,54], we hypothesize that PGEM might activate cGAS-STING pathway. To test this hypothesis, we evaluated the presence of cytosolic DNA and its colocalization with cGAS by picogreen staining and immunofluorescence. Treatment with GEM or PGEM significantly increased the signals of cGAS-bound micronuclei in Panc02 cells compared with control and PVD-treated groups (Fig. 2b). Then, we evaluated the expression of STING pathway-related proteins after various treatments by Western blot. As shown in Fig. 2c, GEM or PGEM treatment significantly induced IRF3 and STING phosphorylation in Panc02 cells. The normalized protein levels of phosphorylated IRF3 (pIRF3) and phosphorylated STING (pSTING) were significantly higher in PGEM- and GEM-treated groups compared with saline and PVD polymer-treated groups (Fig. 2d). These results suggested that treatment with GEM or PGEM was able to activate STING pathway in Panc02 tumor cells. Accumulating evidence has shown that cGAS-STING pathway can be triggered by DNA damage [55,56]. Therefore, we evaluated whether PGEM activated cGAS-STING pathway through inducing DNA damage by using γ H2AX foci as a DNA double strand break (DSB) marker. As shown in Fig. 2e, formation of γ H2AX foci was induced in both GEM- and PGEM-treated Panc02 cells. However, saline- and PVD polymer-treated Panc02 cells displayed no γ H2AX foci. These findings suggested that PGEM and GEM potentially activated the double-strand DNA damage in Panc02 tumor cells *in vitro*, resulting in subsequent activation of cGAS-STING pathway signaling.

It has previously been reported that the cGAS-STING pathway could be activated both in tumor cells and dendritic cells (DC) [57], and activation of STING-IRF3 pathway in DCs is required

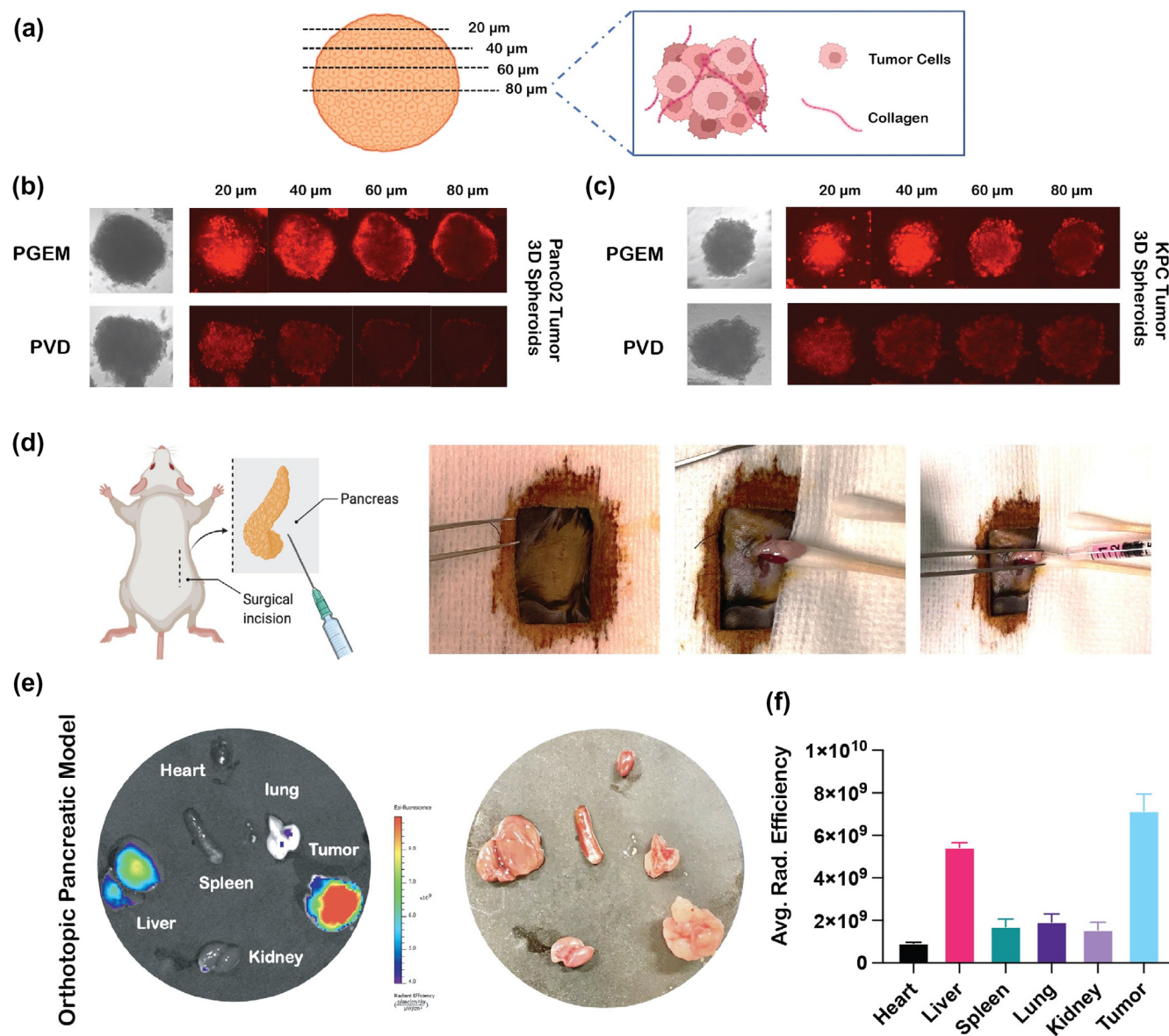
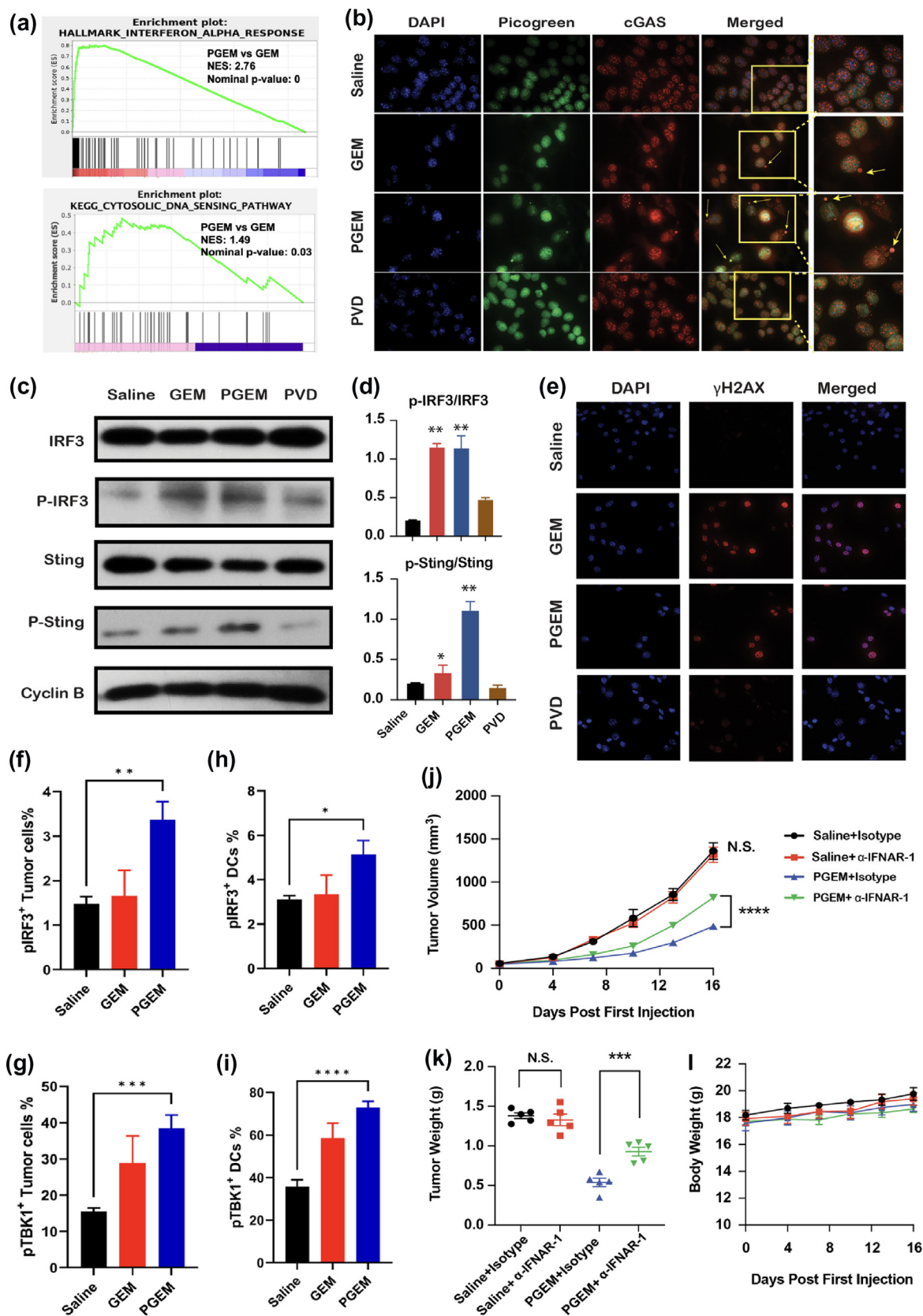


FIG. 1

Deep penetration and widespread distribution of PGEM/DiR micelles in tumor spheroids and orthotopic pancreatic tumors. (a) Schematic illustration of a 3D tumor spheroid consisting of tumor cells and collagen; (b-c) Distribution of the ultra-small sized PGEM (~ 13 nm) and larger sized PVD micelles (~ 160 nm) in panc02 and KPC tumor spheroids after incubation for 16 h; (d) Schematic illustration of establishment of KPC orthotopic pancreatic cancer model; (e) *Ex vivo* NIR imaging of major organs and tumors at 24 h following i.v. injection of DiR loaded PGEM; (f) Quantification of the distribution profile of DiR loaded PGEM in major organs (n = 3).

for antitumor CD8⁺ T cell response [6]. Thus, we investigated whether PGEM activated the STING pathway in both types of cells by flow cytometric analysis of tumor tissues treated with saline, GEM, and PGEM in GFP-Panc02 syngeneic tumor model. As shown in Fig. 2f and g and Fig. S6, PGEM treatments significantly increased the proportion of phosphorylated IRF3 (Ser396, pIRF3⁺) and phosphorylated TBK1-positive (Ser172, pTBK1⁺) tumor cells, suggesting the activation of STING-TBK1-IRF3 signaling in tumor cells *in vivo*, which was consistent with our *in vitro* results. In addition, PGEM treatment significantly increased the proportion of pTBK1- and pIRF3-positive CD11c⁺ CD11b⁻ DCs (Fig. 2h and i and Fig. S6).

To investigate if the cGAS-STING activation by PGEM led to the production of type I IFN, we assessed the *in vitro* and *in vivo* expression of IFN β , a downstream molecule in the STING signaling pathway [57,58]. PGEM significantly increased the mRNA levels of IFN β in both cultured Panc02 cells (Fig. S7a) and harvested tumor tissues (Fig. S7b). We also evaluated whether the efficacy of PGEM therapy is dependent on type I IFNs. The type I IFNs signaling was blocked using antibody against the type I interferon receptor (IFNAR-1). As shown in Fig. 2j-l, PGEM treatment in the presence of blocking antibody led to substantial reduction in therapeutic efficacy of PGEM, demonstrating that PGEM therapy is dependent on type I IFNs.



Taken together, these results indicated that PGEM treatment activated the cGAS-STING pathway and induced type I IFN production, which contributed to the antitumor activity of PGEM. To our knowledge, this is the first study to report that a GEM-based polymer can activate the cGAS-STING pathway. Gao's group reported that another polymer bearing a seven-membered ring with a tertiary amine (PC7A) activated STING pathway through the polymer-induced formation of STING-PC7A condensates, which was cGAS independent [59]. In our case, the STING activation is associated with DNA damage, which facilitates the cytosolic retention of cGAS [60].

STING activation by PGEM led to increased expression of immunosuppressive chemokines

The above RNAseq data clearly showed that PGEM downregulated gene sets involved in PC pathogenesis and activated cGAS-STING innate immune pathway. However, we also observed upregulation of several genes that have been shown to both enhance tumor growth and promote an immunosuppressive TME including CCL2 and CCL7 after treatment with either GEM or PGEM (Fig. 3a-b). It is noted that GEM and PGEM treatments also upregulated the expression of interferon-stimulated gene 15 (ISG15), which is highly correlated with GEM resistance [61]. To validate the RNAseq data, the expression of CCL2, CCL7 and ISG15 was evaluated by qRT-PCR *in vivo* and *in vitro* (Fig. 3c-h). PGEM treatment was more effective in upregulating CCL2, CCL7 and ISG15 expression compared with free GEM in the Panc02 tumor tissues (Fig. 3c-e), while treatment of PVD polymer backbone without GEM showed no obvious changes in these chemokines, indicating that the upregulation is GEM-specific. Notably, PGEM and free GEM similarly induced the expression of CCL2, CCL7 and ISG15 (Fig. 3f-h) in cultured Panc02 cells with free GEM being more effective. This is likely due to the slow release of GEM from PGEM in cultured cells during the limited incubation time while PGEM improves the bioavailability of GEM in tumors *in vivo* by protecting GEM from enzymatic degradation.

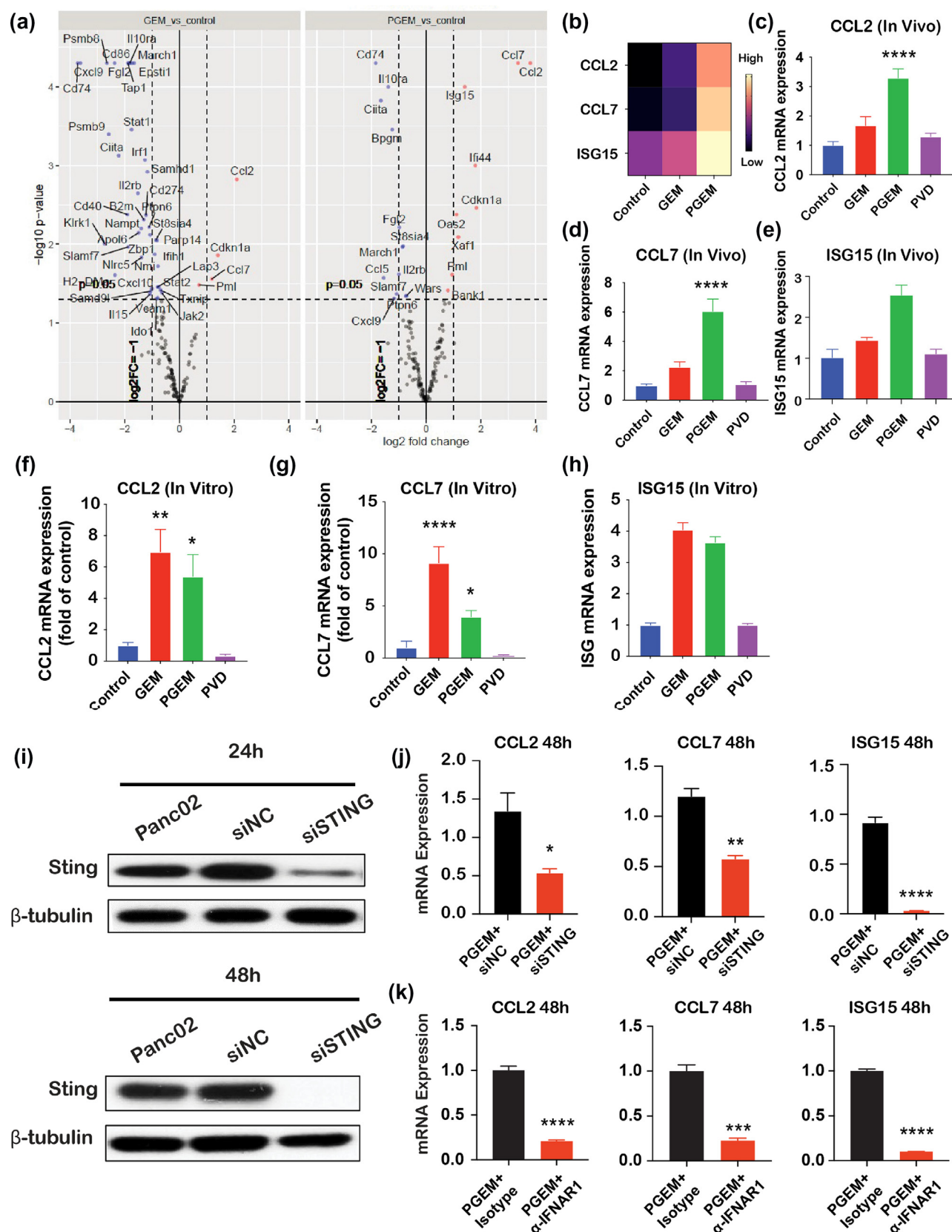
It has been reported that radiation caused CCL2 and CCL7 induction through STING activation [62]. In addition, ISG15 could also be induced by type I interferon (IFN). We hypothesized that activation of cGAS-STING pathway is involved in the PGEM-mediated chemokine induction. To test this hypothesis, we investigated whether knockdown of STING by STING siRNA (siSTING) would decrease the PGEM-induced expression of

CCL2 and CCL7. The efficiency of STING protein expression was confirmed by Western blot in Panc02 cells following treatment with siSTING for 48 h (Fig. 3i). As shown in Fig. 3j, treatment with siSTING significantly attenuated the PGEM-induced expression levels of CCL2, CCL7 and ISG15. We also evaluated whether the induction of CCL2, CCL7 and ISG15 by PGEM was related to the type I IFNs. As shown in Fig. 3k, the expression levels of CCL2, CCL7 and ISG15 in the PGEM-treated Panc02 cells were significantly downregulated in the presence of IFNAR1 neutralization antibody compared to isotype control. These data suggested that the PGEM induced CCL2, CCL7 and ISG15 were STING- and type I IFNs-dependent.

The above data are consistent with the notion that the cGAS-STING pathway is a double-edged sword and the outcome is context-dependent. On the one hand, cGAS-STING pathway has the potential to elicit innate and adaptive immune responses, both of which are critical for cancer immunotherapy [63]. The activation of STING drives the production of cytokines Type I IFNs, which promote the generation of cytotoxic T cell responses as well as type I T helper cell (Th1)-biased responses [64]. Furthermore, type I IFNs promote the activation and functional maturation of DCs, thereby facilitating antigen presentation to CD4⁺ T cells as well as antigen cross-presentation to CD8⁺ T cells [65]. On the other hand, STING activation has been found to promote the proliferation of metastatic cells and chemoresistance in several type of cancers such as breast cancer and lung cancer [66]. In addition, evidence has shown that STING activation induced CCL2 and CCL7 expression, which was associated with immunosuppressive TME due to M-MDSC infiltration, leading to tumor radio-resistance [18]. STING agonist cyclic diadenyl monophosphate (CDA) was also reported to cause induction of other immune regulatory pathways such as cyclooxygenase-2 (COX2) and PD-1 in the TME [67]. Blocking this feedback mechanism via COX-2 inhibition synergized with CDA in inhibiting tumor growth in Lewis lung carcinoma [67]. Clearly, more studies are needed to more comprehensively investigate the negative feedback mechanisms of STING activation and their biological consequences. We demonstrated that PGEM could work as a polymeric STING agonist. Although STING activation likely contributed to the PGEM antitumor activity through the induction of the type I IFN production, it also triggered the undesired induction of CCL2/CCL7. This promoted us to examine the potential of combining PGEM with blockade of CCR2, the receptor shared by both CCL2 and CCL7, in the following studies.

FIG. 2

PGEM treatment activated cGAS-STING signaling pathway. (a) GSEA analysis of upregulated Type I IFN pathway and cGAS-STING pathway; (b) Representative images of picogreen (green) and cGAS (red) stained micronuclei (60 × magnification), the cGAS-bound micronuclei were indicated with arrowheads; (c) Western blotting for phosphorylated IRF3 (pIRF3) and total IRF3 expression as well as phosphorylated STING (pSTING) and total STING expression; (d) Normalized pIRF3 and pSTING protein levels quantified by densitometric analysis; (e) Representative immunofluorescence images of DAPI (blue)- and γH2AX (green)- stained cells with various treatments (20 × magnification); (f-g) Quantification of pIRF3⁺ and pTBK1⁺ tumor cells after various treatments (normalized to saline treated group); (h-i) Quantification of pIRF3⁺ and pTBK1⁺ DCs after various treatments (normalized to saline treated group); (j-l) Panc02 tumor-bearing mice were treated with saline or PGEM micelles (i.v.) plus i.p. injection with anti-IFNAR1 or the isotype control. Tumor sizes and body weight were measured every 4 days (n = 5) and the tumor weight was obtained at the endpoint.



Computer simulation and experimental screening demonstrated that PF-6309 was the optimal CCR2 inhibitor to be loaded into PGEM micelles

There are several CCR2 inhibitors/antagonists currently approved by FDA or in clinical trials, such as PF-04136309 (PF), BMS 813,160 (BMS) and Bindarit (Bind), but the therapeutic efficacies of those compounds are limited by their poor solubility and low bioavailability. Interestingly, PGEM carrier was able to load these inhibitors to form micelles with ultra-small sizes and close-to-neutral zeta potentials (Fig. S8 and S9, Table S3), which well-addressed the solubility and systemic delivery issues.

Current drug formulations are largely developed through trial and error with little insight into the biophysical interaction of drug carriers and loaded drugs. For a rational selection of a CCR2 antagonist that is “optimally” paired with the PGEM-based drug carrier, we applied the state-of-the-art molecular dynamic simulations to study how these three inhibitors interacted with the PGEM polymer. Firstly, we used a series of sequential molecular dynamics (MD) simulations to generate the micelle-like structure formed by a single copy of PGEM polymer, which consists of 32 residues from 4 residue types, including PG (Fig. 4a(i)), NPG (N-terminal PG) (Fig. 4b(ii)), EM (Fig. 4a(iii)), and CEM (C-terminal EM) (Fig. 4a(iv)). To accurately describe the properties of biomolecules in aqueous environment, solvent effects were also considered in the MD simulation. Therefore, we studied the interaction between different CCR2 inhibitors with the PGEM polymer by the combination of Generalized Born molecular dynamics (GBMD) simulation and explicit water MD simulations. Due to highly dynamic attribute of the systems, we calculated radius of gyration (RoG) of the polymer and polymer-drug systems instead of root-mean-square deviation (RMSD), to monitor the conformational change and polymer-drug complex formation (Fig. 4b, Fig. S10). For each MD trajectory, the snapshot which had the smallest RMSD to the average structure was selected as the representative conformation. The representative conformations of the polymer itself and polymer-drug complexes were shown in Fig. 4c and Fig. 4d-f, respectively. Obviously, PF-04136309 can interact with the inside hydrophobic domain of the micelle-like structure by forming T-shape and parallel displaced π - π interactions (Fig. 4g), while the other two drugs have weak interaction with the hydrophobic domain of the polymer.

The “three-trajectories” protocol was used to calculate the binding free energy between the polymer and drug molecules. The MM-PBSA-WSAS free energies of the polymer, the drugs and polymer-drug complexes were listed in Table S4, and the binding free energies were listed in Table S5. The binding free

energies between 8 copies of the drug and the polymer are 5.14, −18.21 and −38.10 kcal/mol for Bindarit, BMS813160, and PF-04136309, respectively. We can also obtain the binding free energies between the polymer and one copy of drug molecule, which are 0.64, −2.28 and −4.76 kcal/mol, correspondingly. The result of MM-PBSA-WSAS free energy analysis is consistent with the MD structures shown in Fig. 4d-g, further confirming that PF-04136309 has much stronger interaction with the PGEM polymer.

Interestingly, we also found that PGEM/PF demonstrated better stability profile in the presence of serum compared to other formulations. As shown in Fig. S11, the PGEM/PF micelles remained stable without significant changes in sizes in 50 % FBS for 48 h. In contrast, PGEM/BMS micelles and PGEM/Bind micelles were not stable and showed increased size at 24 h.

We further assessed the anti-tumor activity of PGEM loaded with PF, BMS, and Bind in the Panc02 tumor bearing mice, respectively. All the formulations showed no obvious toxicity as evident from the slight increases in the body weights of the treated mice (Fig. S12). Among the three agents tested, PF-04136309 showed the best combination effect with PGEM (Fig. 4h). We also compared the *in vitro* cytotoxicity of PGEM/PF with those of other two formulations (PGEM/BMS and PGEM/Bind) (Fig. S13). No significant difference was observed in the cytotoxicity among the three formulations, further indicating that the higher anti-tumor activity of PGEM/PF was likely attributed to the better formulation stability *in vivo* due to the stronger interaction of PF with PGEM. Thus, PF-04136309 was chosen for the subsequent studies.

Our experimental data matched well with the result of MM-PBSA-WSAS analysis. It should be noted that the above study is largely a pilot work of proof-of-principle and the utility of our modeling in selecting optimal drug-drug formulation pair for PGEM/CCR2 antagonist-based as well as other combination therapies warrants more studies in the future.

Loading PF-6309 into PGEM led to improved anti-tumor and anti-metastasis effect

The PF release from PGEM/PF formulation was evaluated *in vitro* by a dialysis method. Free PF was rapidly diffused across the dialysis bag with over 95 % being diffused out of dialysis bag within 24 h. In contrast, PGEM/PF micelles showed a more favorable release kinetics of PF, and only 20 % was slowly released within 72 h (Fig. S14). Due to the chemical conjugation of GEM to the polymer, no detectable GEM was released within 24 h. We also quantitatively evaluated whether PGEM nanocarrier could selectively deliver PF into pancreatic tumors and the retention time of

FIG. 3 PGEM treatment led to enhanced expression of immunosuppressive chemokines via activating STING signaling pathway. (a) Volcano plot showing genes differentially expressed in Panc02 tumors after various treatments; (b) Heat map of chemokines (CCL2, CCL7, and ISG15) expression after various treatments; (c-e) The mRNA expression levels of CCL2 (c), CCL7 (d), and ISG15 (e) in mouse Panc02 tumors treated with saline, GEM, and PGEM for three times; (f-h) The mRNA expression levels of CCL2 (f), CCL7 (g), and ISG15 (h) in cultured Panc02 cell lines treated with saline, GEM, and PGEM; (i) Knock down of STING protein in Panc02 cells assessed by Western blotting after treatments with control siRNA (siNC) or siSTING for 24 h or 48 h; (j) The mRNA expression levels of CCL2, CCL7 and ISG15 after treatments with PGEM plus either siNC or siSTING; (k) The mRNA expression levels of CCL2, CCL7 and ISG15 after treatments with PGEM plus either isotype control or IFNAR1 antibody.

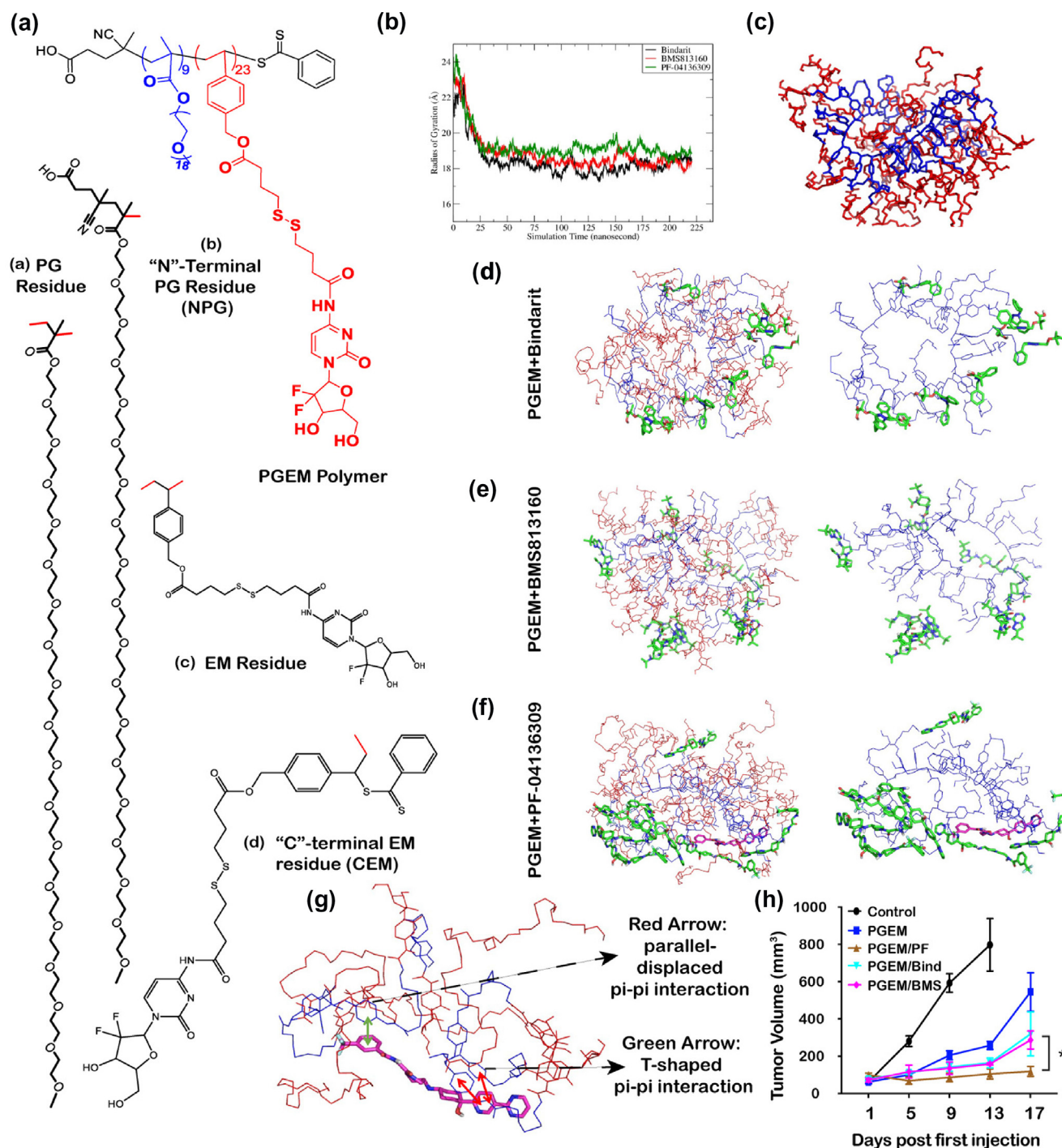


FIG. 4

Computational simulation and experimental screening of optimal CCR2 inhibitor to be loaded into PGEM carrier. (a) the 32-residue PGEM polymer consisted of four types of residues including PG (i), NPG (ii), EM (iii), and CEM (iv). (b) The time courses of radius of gyration of polymer/8-drug systems in explicit water MD simulations. For all the three drugs, RoG reached equilibria after 25 nanoseconds. (c) The representative conformation of the polymer in 200-nanosecond explicit water MD simulations. Hydrophilic and hydrophobic fragments were shown as red and blue sticks, respectively. (d-f) The representative conformation of the polymer/8-Bindarit (d), polymer/8-BMS813160 (e) and polymer/8-PF-04136309 (f) in 220-nanosecond explicit water MD simulations. Drug molecules were shown as greenish sticks. Left: all molecular system; Right: molecular system excluding hydrophilic part. (g) The detailed interaction between one PF-04136309 (sticks) with the polymer (lines). The major contribution of drug-polymer interaction includes a T-shape π - π interaction (double-headed green arrow), and two parallel-displaced π - π interactions (double-headed red arrows). Red arrow: parallel-displaced pi-pi interaction; Green arrow: T-shaped pi-pi interaction. (h) The tumor growth curves after treatments of various CCR2/CCR2 inhibitors formulated in PGEM micelles.

PF in the tumor tissues via UPLC-MS. As shown in Fig. S15, higher amount of PF was detected in the tumors compared to other organs, suggesting that PGEM nanocarrier was able to selectively deliver PF to the tumor sites. Compared to the kinetics of DiR in tumors (Fig. S3), PF showed a relatively faster clearance in tumors (Fig. S16) likely due to a relatively rapid metabolism of PF in tumor tissues.

Then, we evaluated the therapeutic efficacy of PGEM/PF both *in vitro* and *in vivo*. The combination effect of free PF and GEM as well as PGEM/PF formulation in cytotoxicity was firstly examined in Panc02 cells (Fig. S17). Free PF showed slight cytotoxicity *in vitro*. Compared to free GEM, combination of PF with GEM increased the overall cytotoxicity, indicating that PF could sensitize the pancreatic tumor cells to GEM treatment. Compared to PGEM, incorporation of PF into PGEM carrier significantly enhanced the cytotoxicity at high concentrations.

We also evaluated the combination effect of free PF and GEM *in vivo*. As shown in Fig. 5a, free PF or GEM alone showed modest effect in inhibiting the growth of Panc02 tumor. Combination of the two drugs led to improvement in the overall therapeutic efficacy, suggesting their potential combination/synergistic effect. Then, we evaluated whether loading PF into PGEM carrier further improved the therapeutic efficacy. As shown in the Fig. 5b, PGEM showed a therapeutic efficacy that was comparable to that of free PF and GEM combination. PF formulated in the PGEM carrier drastically enhanced the therapeutic efficacy of PGEM. This was further confirmed by the lowest tumor weights at the end point (Fig. 5c). We further examined the tumor histology at the end of the experiment. As shown in Fig. 5d, H&E-stained tumor sections in the saline-treated group showed typical high density of tumor cells with large nuclei. In comparison, the tumor sections in other treatments showed areas of necrosis. In addition, altered morphology of cancer cells with shrunk nuclei and cell damage was observed as well. Among all the four treatment groups, PGEM/PF micelles exhibited the most significant intra-tumor tissue damage.

There were no obvious changes in the mouse body weights following various treatments (Fig. 5e). Furthermore, these treatments had no effect on liver and kidney functions as evident from little changes in serum levels of alanine aminotransferase (ALT), aspartate aminotransferase (AST) and creatinine (Fig. 5f). In addition, there were no obvious changes in white blood cell (WBCs), red blood cells (RBCs), hemoglobin concentrations, lymphocytes, monocytes and other immune cells (leukocytes) in peripheral blood after treatment with PGEM/PF in comparison to control group (Fig. 5g-k, Fig. S18). Finally, no obvious changes were found in histology for all major organs examined including heart, liver, spleen, lung, and kidney after different treatments (Fig. S19). These data suggested the excellent safety profile of the PGEM/PF at a dosage that demonstrated significant therapeutic efficacy.

As metastasis is one of the leading causes of death in pancreatic cancer patients, we also evaluated the anti-metastasis effect of PGEM/PF in a murine pulmonary metastasis model of pancreatic cancer. As shown in Fig. 5l, PGEM showed an anti-metastasis efficacy that was comparable to that of free PF and GEM combination. PGEM/PF micelles drastically controlled the metastasis of pancreatic cancer. This was further confirmed by the fewest

tumor nodules at the end time point (Fig. 5m). We further examined the lung histology at the end of the experiment. As shown in Fig. 5n and o, PGEM/PF-treated group showed significantly less density of tumor cell infiltration in the lung compared to other groups, further suggesting better anti-metastasis effect of PGEM/PF combination.

The enhanced inhibition of tumor growth by PGEM/PF was translated into a prolongation in survival time (Fig. S20). Among different treatments, PGEM/PF led to longer survival rate of the mice, further suggesting its excellent therapeutic outcomes.

Loading PF-6309 into PGEM led to improved tumor immune microenvironment

The impact of PGEM/PF on tumor immune microenvironment was further investigated by flow cytometric analysis of harvested tumors after various treatments. As shown in Fig. 6a-c and Fig. S21, PGEM treatment led to a drastic increase in the percentage of MDSCs and TAMs, which might be attributed to the upregulation of CCL2 and CCL7 as described above. It is also apparent that free PF and PGEM/PF treatments led to a decrease in the percentage of MDSCs and TAMs. Interestingly, PGEM/PF treatment led to a decrease in the percentage of M2 type macrophages, along with an increase in the percentage of M1 type macrophages and M1/M2 ratios, suggesting that the tumor infiltrating macrophages were polarized from a tumor-promoting to a tumor-suppressing phenotype. These results indicated that incorporation of PF into PGEM could reverse the MDSCs- and TAMs- immunosuppression induced by the PGEM.

Natural Killer (NK) cells are lymphocytes involved in the early innate immune response. As shown in Fig. 6d-f and Fig. S22, there was a significant increase in the total percentage of NK cells in the tumors after the treatments with free PF + GEM combination, PGEM, and PGEM/PF. Moreover, the numbers of IFN- γ ⁺ NK and GZB⁺ NK cells were significantly increased in the tumors treated with PGEM/PF in comparison to all the other treated groups. It is known that IFN- γ and GZB are pleiotropic cytokines that can eliminate tumor cells directly and indirectly [26]. Therefore, PGEM/PF treatment increased the number of functional NK cells in the tumors. CD8⁺ T cells are critically involved in the adaptive immune response against cancer. As shown in Fig. 6g-h and Fig. S23, all treatments increased the percentages of CD8⁺ T cells in the tumors. Compared to PGEM treatment, incorporation of PF into PGEM carrier further increased the percentages of CD8⁺ T cells in the tumors. In addition, PGEM/PF was highly effective in increasing the number of functional CD8⁺ T cells (GZB⁺ CD8⁺ T cells) (Fig. 6h). The above data demonstrated remarkable changes in the immune landscape of PDAC tumors after PGEM/PF treatment.

To characterize the role of NK and CD8⁺ T cells in the significant tumor inhibition effect of PGEM/PF treatment, neutralizing monoclonal antibodies (mAbs) were used to deplete NK and CD8⁺ T cells. Similar to the data shown in Fig. 5b, PGEM/PF treatment led to significant growth inhibition of Panc02 tumors that received IgG isotype controls. In contrast, injection of either anti-NK or anti-CD8 mAb significantly attenuated the tumor growth inhibition in the PGEM/PF-treated mice (Fig. 6i-l, Fig. S24, and Fig. S25). This implies that both NK cells and cyto-

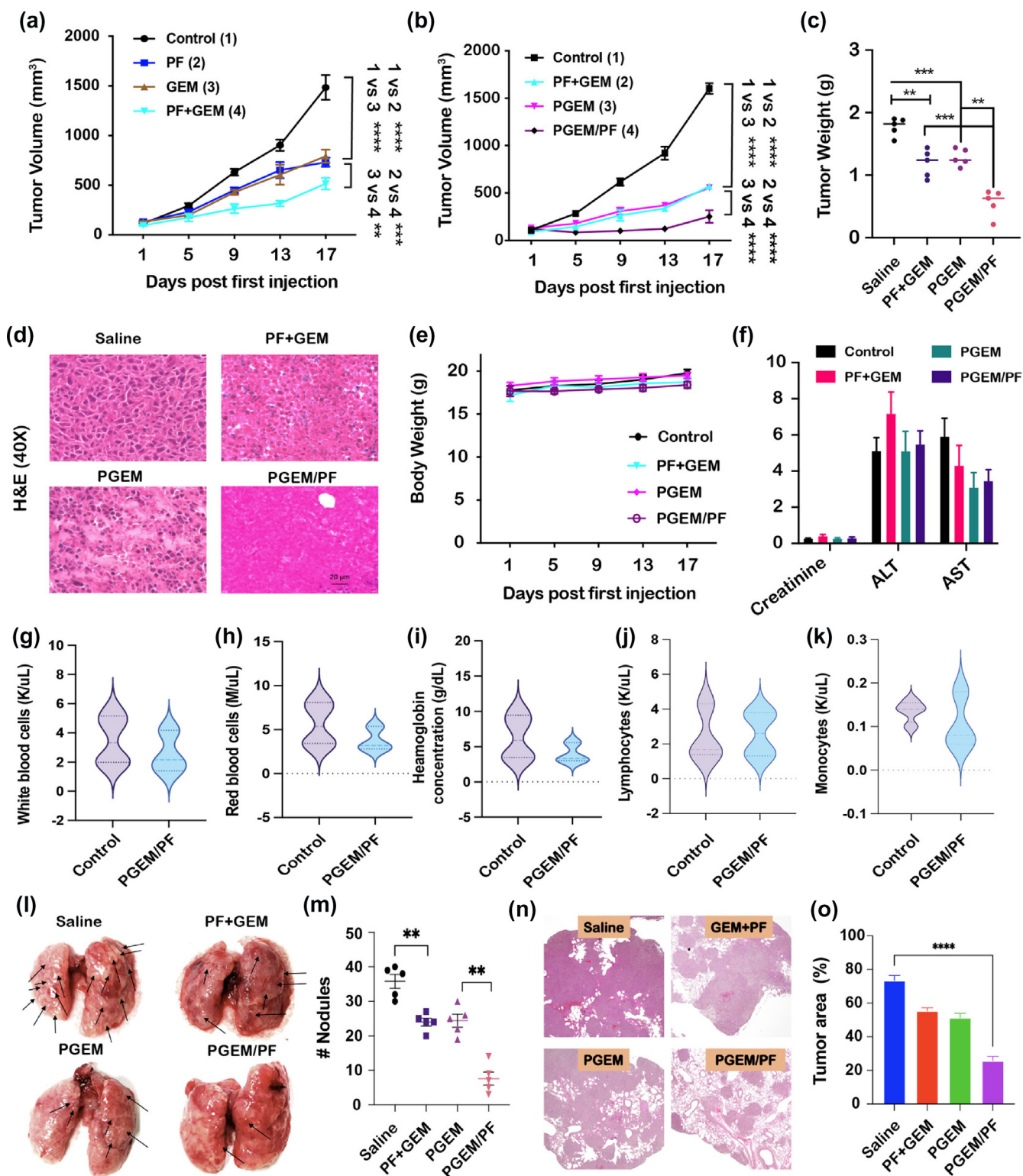


FIG. 5

PGEM/PF-6309 micelles exhibited potent anti-tumor efficacy. (a) tumor growth curve after combination of GEM and PF; (b-c) tumor growth curve after various treatments and tumors were weighed at the completion of the experiment; (d) H&E staining after various treatments (Scale bar: 20 μ m); (e-k) safety profile of PGEM/PF micelles including body weight (e), kidney and liver function (f), white blood cell (WBCs) (g), red blood cells (RBCs) (h), hemoglobin concentrations (i), lymphocytes (j), and monocytes (k) in peripheral blood. (l-o) PGEM/PF micelles suppressed lung metastasis of pancreatic cancer *in vivo*. (l) representative lung images; (m) the number of tumor nodules in lung tissues; (n) H&E staining of lung tissues at the endpoint; (o) quantification of tumor areas of H&E images following various treatments.

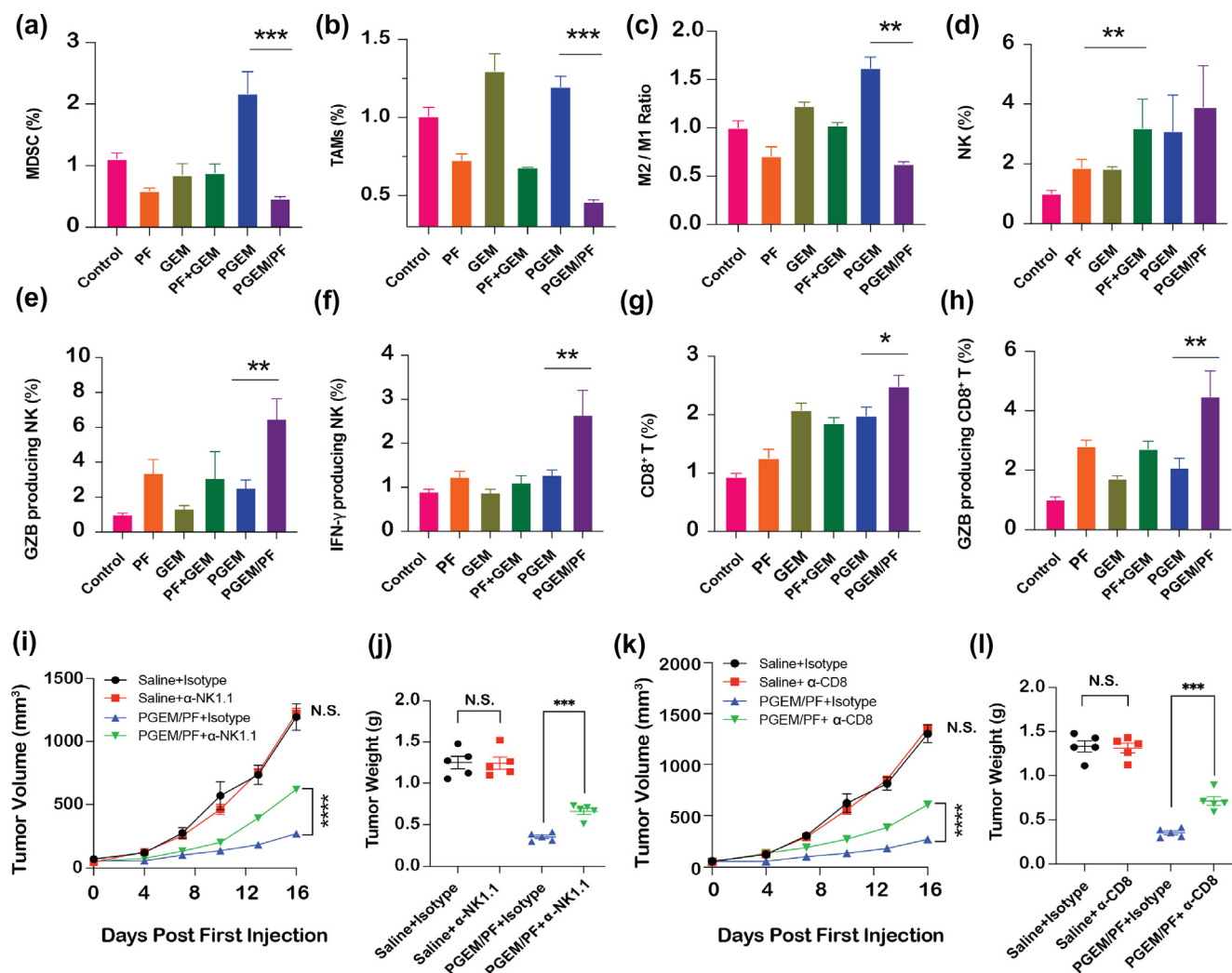


FIG. 6

PGEM/PF-6309 micelles exhibited potent anti-tumor efficacy by activating innate and adaptive immunity. (a-h) immune profiling after various treatments. Percentages of Myeloid Derived Suppressive Cells (MDSCs) (a) and Tumor Associated Macrophages (TAMs) (b); M2/M1 ratios (c); percentages of natural killer (NK) cells (d), GZB producing NK cells, and IFN-γ producing NK cells; percentages of CD8⁺ T cells and GZB producing CD8⁺ T cells. Percentages are normalized to control group. (*P < 0.05; **P < 0.01; ***P < 0.001). Panc02 tumor bearing mice were treated with saline or PGEM/PF micelles (i.v.) plus i.p. injection with anti-NK1.1 (i-j) and anti-CD8 (k-l), or their isotype controls. Tumor sizes were measured every 4 days (n = 5) and the tumor weight was obtained at the endpoint.

toxic CD8⁺ T cells contributed significantly to the antitumor immunity in PGEM/PF treated mice.

PGEM/PF-6309 formulation sensitized PDAC to anti-PD-1 therapy

Although PGEM/PF treatment led to an immune-active TME, it also triggered concurrent induction of immune checkpoint molecules. FACS showed significant up-regulation of PD-1 expression in NK cell and CD8⁺ T cells (Fig. 7a-d) in tumors after PGEM/PF treatment. Therefore, we hypothesized that the tumor growth inhibition after PGEM/PF treatment can be further improved through combination with anti-PD-1 immune checkpoint blockade (ICB) (Fig. 7e). As shown in Fig. 7f-h, compared to PGEM/PF and anti-PD-1 alone, the combination treatment led to significantly improved inhibition effect on tumor growth

(Fig. 7f-h). One out of the 5 tumors completely regressed, clearly demonstrating the remarkable therapeutic benefit of combining the two treatments (Fig. 7h).

Conclusions

Guided by RNAseq and computer modeling, a new immunochemotherapy for PDAC was developed by incorporating a CCR2 antagonist PF-6309 into a GEM prodrug (PGEM)-based ultrasmall nanocarrier. PGEM nanocarrier showed excellent tumor penetration in pancreatic tumor spheroids and in a KPC orthotopic tumor model. The PGEM carrier itself could activate cGAS-STING signaling pathway in both pancreatic tumor cells and DCs, and mediated potent anti-tumor immune response. More specifically, PGEM promoted the recruitment of more tumor-infiltrating NK cells and CD8 T cells and led to

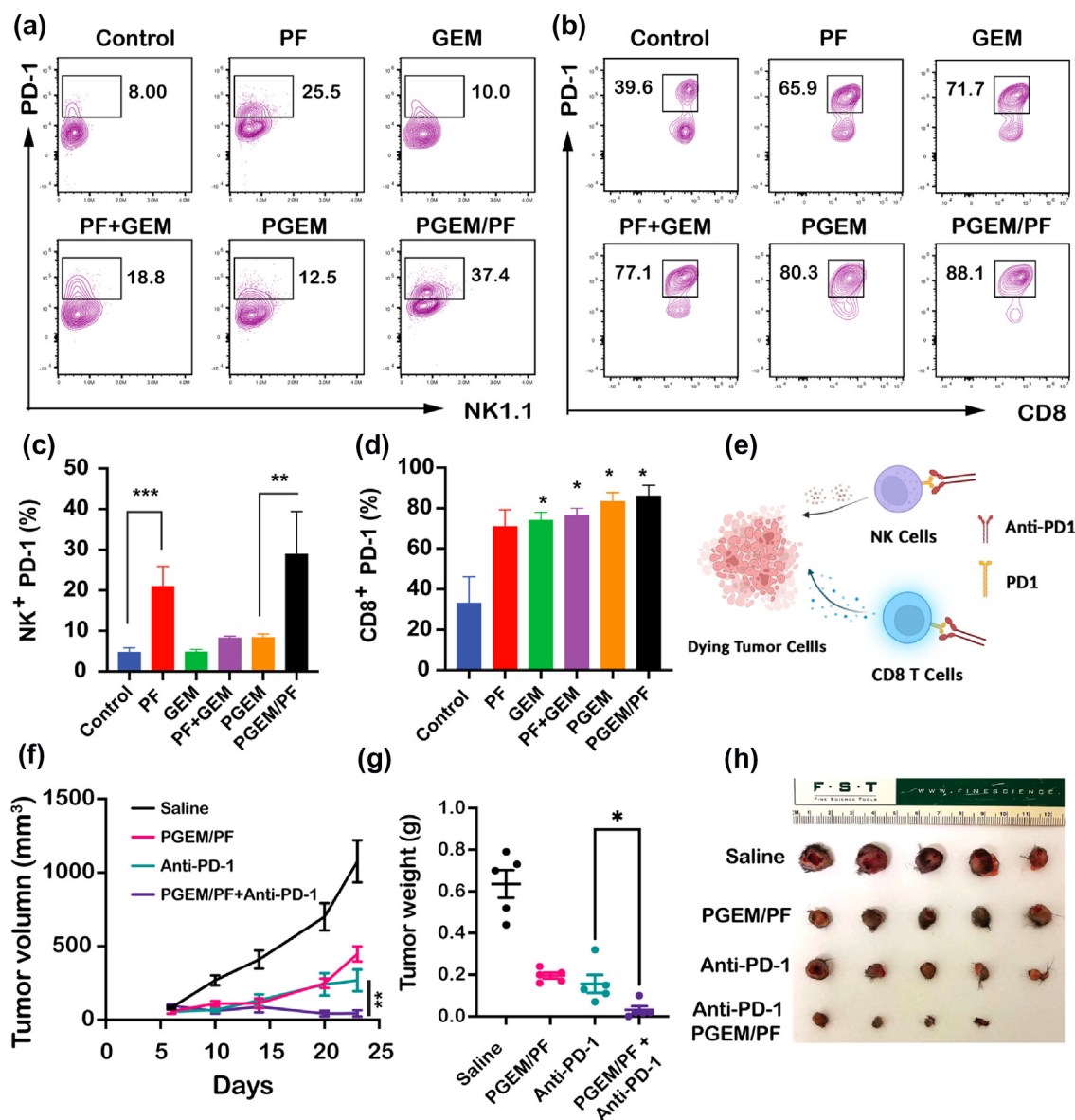


FIG. 7

PGEM/PF micelles synergized with Anti-PD-1 treatment. (a-d) Representative flow cytometric plots and the quantification of the percentages of PD-1⁺ cells within the gated NK1.1⁺ and CD8⁺ T populations in Panc02 tumors; (e) Illustration of rationale for PGEM/PF micelles in combination with anti-PD-1 regimen; (f-h) Therapeutic effect of various formulations. Female C57BL/6 mice were subcutaneously inoculated with equal numbers of panc02 tumor cells and received various treatments respectively, and tumor growth was followed every 4 days (f). Tumors were weighed at the completion of the experiment (g) and the representative images have been obtained (h).

increased production of IFN- γ and GZB in those two cell populations. We also found that PGEM treatment upregulated the expression of chemokines CCL2 and CCL7, which induced immune resistance by recruiting more M2 associated macrophage and MDSCs. Incorporating PF-6309 into PGEM carrier significantly altered the tumor immune microenvironment by reversing the immunosuppression mediated by M2 and MDSCs while maintaining the effective tumor-infiltration of NK cells and CD8 T cells, which led to amplified anti-tumor immunity and enhanced anti-tumor response. Furthermore, PGEM/PF formulation sensitized PDAC tumors to anti-PD-1 therapy and the combination treatment led to significant suppression/eradica-

tion of the tumors. In summary, our work discovered a new polymer-based STING agonist and provided a rationally designed formulation for enhanced PDAC immunotherapy.

CRedit authorship contribution statement

Zhuoya Wan: Data curation, Formal analysis, Methodology, Validation, Visualization, Writing – original draft, Writing – review & editing, Software, Investigation. **Haozhe Huang:** Investigation, Validation, Visualization. **Raymond E. West III:** Investigation, Validation, Writing – review & editing. **Min Zhang:** Data curation, Software, Formal analysis, Visualization,

Writing – review & editing. **Bei Zhang:** Investigation, Validation, Visualization. **Xinran Cai:** Investigation. **Ziqian Zhang:** Investigation, Validation. **Zhangyi Luo:** Investigation. **Yuang Chen:** Investigation. **Yue Zhang:** Investigation. **Wen Xie:** Writing – review & editing. **Da Yang:** Writing – review & editing. **Thomas D. Nolin:** Resources, Writing – review & editing. **Junmei Wang:** Resources, Data curation, Formal analysis, Methodology, Validation, Visualization, Writing – original draft, Writing – review & editing, Software, Investigation. **Song Li:** Conceptualization, Supervision, Writing – review & editing, Resources, Funding acquisition. **Jingjing Sun:** Conceptualization, Supervision, Investigation, Writing – original draft, Writing – review & editing, Resources, Funding acquisition.

Declaration of Competing Interest

The authors declare the following financial interests/personal relationships which may be considered as potential competing interests: The authors declare the following competing financial interest(s): Song Li serves on the Chief Scientific Officer and holds equity in DUO Oncology. Jingjing Sun is an inventing consultant and equity holder in DUO Oncology.

Acknowledgement

This work was supported by the fund from National Institute of Health grants R01CA174305, R01CA219399, R01CA223788 (to SL), R21CA249649 (to JS), S10OD028540 (to TN), a grant from Shear Family Foundation (SL, USA), and the National Science Foundation (NSF1955260 to JW). The authors also acknowledge the support of the Health Sciences Small Molecule Biomarker Core and thank the computing resources provided by the Center for Research Computing (CRC) at University of Pittsburgh.

Appendix A. Supplementary material

Supplementary data to this article can be found online at <https://doi.org/10.1016/j.mattod.2022.11.008>.

References

- [1] K.D. Miller et al., *CA Cancer J Clin* 66 (4) (2016) 271.
- [2] J. Watt, H.M. Kocher, *Oncoimmunology* 2 (12) (2013) e26788.
- [3] G.J. Weiss et al., *Br J Cancer* 117 (1) (2017) 33.
- [4] T.F. Gajewski, et al., (2017), 19.
- [5] L. Sun et al., *Science* 339 (6121) (2013) 786.
- [6] S.-R. Woo et al., *Immunity* 41 (5) (2014) 830.
- [7] L. Corrales, T.F. Gajewski, *Clin Cancer Res* 21 (21) (2015) 4774.
- [8] S. Crunkhorn, *Nat Rev Immunol* 20 (10) (2020) 589.
- [9] L. Motedayen Aval et al., *J Clin Med* 9 (10) (2020) 3323.
- [10] L. Zhou et al., *Cancer Lett* 500 (2021) 163.
- [11] G. Pépin et al., *MBio* 8 (5) (2017) e01611.
- [12] J. Ahn et al., *Cancer Cell* 33 (5) (2018) 862.
- [13] T.F. Gajewski, E.F. Higgs, *Science* 369 (6506) (2020) 921.
- [14] E.N. Chin et al., *Science* 369 (6506) (2020) 993.
- [15] D. Shae et al., *Nat Nanotechnol* 14 (3) (2019) 269.
- [16] J.T. Crowl et al., *Annu Rev Immunol* 35 (2017) 313.
- [17] K.W. Chung et al., *Cell Metab* 30 (4) (2019) 784.
- [18] H. Liang et al., *Nat Commun* 8 (1) (2017) 1.
- [19] Y. Liu et al., *PeerJ* 6 (2018) 4928.
- [20] T.M. Nywening et al., *Gut* 67 (6) (2018) 1112.
- [21] M. Noel et al., *Invest New Drugs* 38 (3) (2020) 800.
- [22] J. Sun et al., *Theranostics* 10 (3) (2020) 1136.
- [23] Y. Liu et al., *Biochem Pharmacol* (2021) 114453.
- [24] J. Li et al., *Immunity* 49 (1) (2018) 178.
- [25] X. Liu et al., *J Clin Invest* 127 (5) (2017) 2007.
- [26] A. Dobin et al., *Bioinformatics* 29 (1) (2013) 15.
- [27] B. Li, C.N. Dewey, *BMC Bioinf* 12 (2011) 323.
- [28] C. Trapnell et al., *Nat Biotechnol* 31 (1) (2013) 46.
- [29] A. Subramanian et al., *Proc Natl Acad Sci U S A* 102 (43) (2005) 15545.
- [30] V.K. Mootha et al., *Nat Genet* 34 (3) (2003) 267.
- [31] J. Wang et al., *J Comput Chem* 25 (9) (2004) 1157.
- [32] , Wallingford, CT, 2016.
- [33] J. Wang et al., *J Mol Graph Model* 25 (2) (2006) 247.
- [34] , University of California, San Francisco, 2018.
- [35] W. Rocchia et al., *J Phys Chem B* 105 (28) (2001) 6507.
- [36] L. Li et al., *BMC Biophys* 5 (1) (2012) 1.
- [37] J. Wang et al., *Curr Comput Aided Drug Des* 2 (3) (2006) 287.
- [38] E. Wang et al., *Chem Rev* 119 (16) (2019) 9478.
- [39] J. Wang, T. Hou, *J Chem Inf Model* 52 (5) (2012) 1199.
- [40] J. Sun et al., *Acta Biomater* 106 (2020) 289.
- [41] Z. Wan et al., *Science, Advances* 7 (50), eabj4226 (2021).
- [42] E.L. Dane et al., *Nat Mater* 21 (6) (2022) 710.
- [43] L. Cheradame et al., *Oncogene* 40 (49) (2021) 6627.
- [44] H. Burris 3rd et al., *J Clin Oncol* 15 (6) (1997) 2403.
- [45] H. Maeda et al., *Adv Drug Deliv Rev* 65 (1) (2013) 71.
- [46] M.K. Danquah et al., *Adv Drug Deliv Rev* 63 (8) (2011) 623.
- [47] F. Danhier et al., *J Control Release* 148 (2) (2010) 135.
- [48] V.P. Chauhan, R.K. Jain, *Nat Mater* 12 (11) (2013) 958.
- [49] A.D. Rhim et al., *Cancer Cell* 25 (6) (2014) 735.
- [50] D.H. Von et al., *N Engl J Med* 369 (18) (2013) 1691.
- [51] H. Cabral et al., *Nat Nanotechnol* 6 (12) (2011) 815.
- [52] J. Gao et al., *Am J Cancer Res* 7 (2) (2017) 173.
- [53] Q. Chen et al., *Nat Immunol* 17 (10) (2016) 1142.
- [54] J. Kwon, S.F. Bakhom, *Cancer Discov* 10 (1) (2020) 26.
- [55] T. Li, Z.J. Chen, *J Exp Med* 215 (5) (2018) 1287.
- [56] C. Li et al., *Mol Immunol* 131 (2021) 180.
- [57] L. Corrales et al., *J Clin Invest* 126 (7) (2016) 2404.
- [58] D. Bose, *Int J Mol Sci* 18 (11) (2017) 2456.
- [59] S. Li et al., *Nat Biomed Eng* 5 (5) (2021) 455.
- [60] H. Liu et al., *Nature* 563 (7729) (2018) 131.
- [61] S. Ina et al., *Pancreas* 39 (4) (2010) 473.
- [62] S. Feng et al., *Nat Commun* 8 (1) (2017) 1.
- [63] T. Su et al., *Theranostics* 9 (25) (2019) 7759.
- [64] D.F. Tough, *Immunol Cell Biol* 90 (5) (2012) 492.
- [65] M.P. Longhi et al., *J Exp Med* 206 (7) (2009) 1589.
- [66] Q. Chen et al., *Nature* 533 (7604) (2016) 493.
- [67] H. Lemos et al., *J Immunother Cancer* 8 (2020) 2.